A new homobimetallic cobalt(II) complex based on the tetradentate 3,5-bis(2-pyridyl)-1H-1,2,4-triazole ligand: Synthesis, crystal structure, Hirshfeld analysis, spectroscopic characterization, magnetic properties and antimicrobial activities

Olivier Mentré, Abdelhakim Laachir, Salaheddine Guesmi, El Mostafa Ketatni, Mohamed Saadi, Lahcen El Ammari, Siham Esserti, Mohammed Faize, Fouad Bentiss

New homobimetallic cobalt(II) complex based on tetradentate 3,5-bis(2-pyridyl)-1H-1,2,4-triazole ligand: Synthesis, crystal structure, Hirshfeld analysis, spectroscopic characterizations, magnetic property and antimicrobial activities

Abdelhakim Laachir [a,b], Salaheddine Guesmi [a], El Mostafa Ketatni [c], Mohamed Saadi [d], Lahcen El Ammari [d], Olivier Mentré [e], Siham Esserti [f], Mohammed Faize [f], Fouad Bentiss [b,*]

[a] *Laboratory of Coordination and Analytical Chemistry (LCCA), Faculty of Sciences, Chouaib Doukkali University, PO Box 20, M-24000 El Jadida, Morocco*
[b] *Laboratory of Catalysis and Corrosion of Materials (LCCM), Faculty of Sciences, Chouaib Doukkali University, PO Box 20, M-24000 El Jadida, Morocco*
[c] *Laboratory of Organic and Analytical Chemistry, Faculty of Science and Technology, Sultan Moulay Slimane University, PO Box 523, Beni-Mellal, Morocco*
[d] *Laboratoire de Chimie Appliquée des Matériaux, Centre des Sciences des Matériaux, Faculty of Science, Mohammed V University in Rabat, Avenue Ibn Batouta, B.P. 1014, Rabat, Morocco*
[e] *Univ. Lille, CNRS, Centrale Lille, UMR 8181, - UCCS - Unité de Catalyse et de Chimie du Solide, F-59000 Lille, France*
[f] *Laboratory of Plant Biotechnology, Ecology and Ecosystem Valorisation, Faculty of Sciences, Chouaib Doukkali University, PO Box 20, M-24000 El Jadida, Morocco*

* Corresponding author. fbentiss@gmail.com

ABSTRACT

A novel homobimetallic cobalt(II) complex, $[Co_2(bpt)_2(H_2O)_4](NO_3)_2.2H_2O$ (bpt = 3,5-bis(2-pyridyl)-1,2,4-triazolate), has been synthesized and characterized by single crystal X-ray diffraction, Hirshfeld surface analysis, as well as UV-Visible, and FTIR techniques. The crystal structure determination shows that the dinuclear complex crystallizes in triclinic crystal system with $P\bar{1}$ space group. The $(N',N^1,N^2,N'')_2$ double bridging coordination mode is realised with distorted octahedral N_4O_2-coordinated cobalt. The structure cohesion is ensured by different intermolecular hydrogen bonds, π–π stacking interactions and by intermolecular lone-pair$\cdots\pi$ interactions. The structure consists of dimeric units $[Co_2(bpt)_2]^{2+}$ with a cobalt-cobalt distance of 4.170(2) Å. Magnetic measurements carried out on the homobimetallic complex indicate a relatively weak antiferromagnetic interaction between the two cobalt centres. This complex exhibited antimicrobial activity against several strains of the fungal phytopathogens *Verticillium dahliae* and *Fusarium oxysporum* fsp. *melonis* as well as against the phytopathogenic bacteria *Agrobacterium tumefaciens*, suggesting its use in crop protection.

Keywords: 3,5-Bis(2-pyridyl)-1,2,4-triazolate; Homobimetallic Co^{II} complex; Crystal structure; Hirshfeld surface analysis; Magnetic property; Antimicrobial activity.

1. Introduction

There is interest in dimeric complexes of odd electron metals with close metal-metal contacts and appropriate bridging atoms for their magnetic properties [1-11]. These properties may be modified by the character of the bridging species and by the geometry of the metal atoms and organic ligands. Thus there is an interest in multidentate ligands which may serve to orient the d orbitals of the two metals to achieve maximum interaction. 1,2,4-Triazole and its derivatives are very interesting chelating ligands, which represent a hybrid of pyrazole and imidazole and are able to act as bridges between metal centers [2,3,12]. 1,2,4-Triazoles with o-pyridine substitution at the 3 and 5 positions may serve as appropriate matrix ligands in either neutral or anionic form (Scheme 1). When one of the three nitrogen atoms of the 1,2,4-triazole ring bears an hydrogen, the ligand is neutral, it's the 3,5-bis(pyridin-2-yl)-1H-1,2,4-triazole abbreviated as Hbpt. This laster can be often deprotonated to form an anionic 3,5-bis(2-pyridyl)-1,2,4-triazolate (bpt) in the formation process of complexes. However, only few mono or dinuclear transition metal complexes as well as tetranuclear or even polymeric complexes containing anionic bpt ligand were characterized by X-ray diffraction [4,6,7,12-20], which indicate that these coordination compounds have relatively poor crystallization behaviour. Different coordination modes can be occurred with bpt ligand and transition metal (Scheme 2). Indeed, when the four nitrogen atoms *N*', N^1, N^2 et *N*'' of the btp ligand are on the same side, a double-bridged bimetallic complex in close proximity is obtained (cisoid conformation); with metal-to-metal distance varying approximately from 4 to 4.5 Å [7,12,16,19,20]. In contrast, when one pyridine ring rotates 180° to chelate a metal ion with the contribution of the nitrogen atom in position 4, a mono-briged bimetallic complex is obtained (transoid conformation) [15,21,22]. Generally, bpt complexes would prefer the cisoid conformation [16].

Moreover, bpt ligand has formed complexes with appropriate transition metals (M) displaying either antiferromagnetic or ferromagnetic behaviour [12,17]. Magnetic exchange

involving the M–N=N–M bridge has been postulated to imply a σ overlap superexchange pathway exploiting the electrons of the heterocyclic ligands [17]. Spin crossover from one magnetic behaviour to the other has been observed with iron(II) complexes based on 3,5-di(2-pyridyl)-1,2,4-triazoles and 3,5-di(2-pyridyl)-1,2,4-triazolates ligands [7]. Structural parameters such as the coplanarity of metal and heteroatom containing ligand, and the magnitude of the M–N=N angles have been discussed as playing a role in the magnetic comportment [19]. In addition, the triazoles and their complexes possess a variety of interesting biological activities, such as anticonvulsant, antifungal, anticancer, anti-inflammatory and antibacterial properties [23–26].

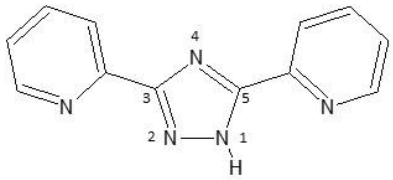

Hbpt

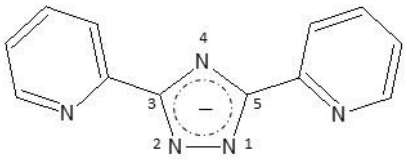

bpt

Scheme 1. 3,5-Bis(2-pyridyl)-1H-1,2,4-triazole (Hbpt) and its anionic form (bpt).

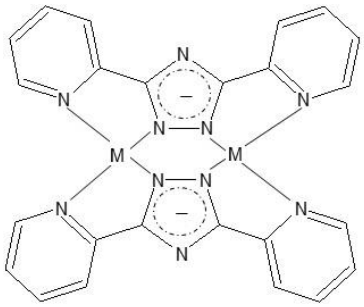

Dinuclear (N',N^1,N^2,N'')$_2$ double bridging
(cisoid form)

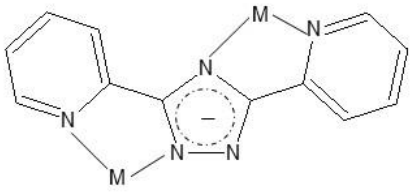

Dinuclear N',N^1,N^2,N'' single bridging
(transoid form)

Scheme 2. The coordination modes of bpt.

In view of these reports and as part of our going researches on the synthesis, structural investigation and property of heterocyclic metal complexes, we have chosen Hbpt as a bridging ligand to construct novel homobimetallic cobalt complex. We report herein the synthesis, structural and spectroscopic characterizations, and Hirshfeld surface analysis, as well as magnetic property and antimicrobial activity of dinuclear cobalt(II) nitrate complex with 3,5-bis(2-pyridyl)-1,2,4-triazolate (bpt), $[Co_2(bpt)_2(H_2O)_4](NO_3)_2.2H_2O$.

2. Experimental

2.1. Materials

The ligand, namely 3,5-bis(2-pyridyl)-1H-1,2,4-triazole (Hbpt) was synthesized according to the literature procedure [24]. The molecular structure of Hbpt is shown in Scheme 1. All the solvents and reagents for synthesis were commercially available and used as received.

2.2. Synthesis of the title compound $[Co_2(bpt)_2(H_2O)_4](NO_3)_2.2H_2O$

A solution of Hbpt (22.3 mg, 0.1 mmol) in EtOH (20 mL) was added to an aqueous solution (5 mL) of $Co(NO_3)_2.6H_2O$ (29.1 mg, 0.1 mmol) with stirring. After that, a solution of NaOH (0.1N, 5ml) was added to the resulting mixture. The solution was stirred at 50 °C during 2 h and filtered. On cooling and slow evaporation, red block crystals suitable for X-ray structural determination were formed after standing over a period of two weeks, which were filtered off, washed with water and dried under vacuum. (yield~65% based on Co). Elemental analysis calcd. (%) for $C_{24}H_{28}Co_2N_{12}O_{12}$: C, 36.29; H, 3.55; N, 21.16. Found: C, 36.26; H, 3.48; N, 21.13%. FTIR (KBr pellet, cm^{-1}): 3400 (w), 3066 (vw), 1648 (vs), 1636 (w), 1600 (m), 1584 (m), 1432 (s), 1387 (w), 1147 (w), 786 (s), 694 (vs). UV–vis (λ_{max}, nm (ε_{max}, M^{-1} cm^{-1})) in DMSO: 785 (50), 509 (1290), 479 (1040), 260 (10600), 236 (7700).

2.3. Single crystal X-ray data collection

A suitable single crystal for X-ray diffraction analysis of the title compound was selected under a microscope (0.33 × 0.29 × 0.25 mm). The red single crystal for the X-ray diffraction (XRD) data collection was mounted on a Bruker APEX-II CCD diffractometer equipped with a CCD bi-dimensional detector and MoK_α graphite-monochromatic radiation (λ = 0.71073 Å). SAINT$^+$ 6.02 program was used for extraction and integration of diffraction intensities [28] and SADABS program was carried out for correction of absorption effect [29]. The coordination complex structure was solved by direct methods using SHELXTL-2014/4 [30] and refined (by weighted full matrix least-square on F^2 techniques) to convergence using the SHELXL-2016/6 program [31]. All non-hydrogen atoms were refined anisotropically. Hydrogen atoms were located in a difference map and treated as riding with C–H = 0.96 Å for the aromatic CH, with U_{iso}(H) = 1.2 U_{eq} (aromatic). Crystal data, data collection and structure refinement details are summarized in Table 1. The bond distances and angles are given in Table 2. The plot of the title complex and the three-dimensional drawing of the crystal structure are obtained using the Ortep3 and Mercury programs, respectively [32,33].

2.4. Hirshfeld surface analysis

The Hirshfeld surfaces calculated for the title complex provide additional information on the distinctive contributions made to the molecular packing. Thus, a Hirshfeld surface analysis [34] and the associated two-dimensional fingerprint plots [35] were performed using CrystalExplorer17.5 [36] to figure out the normalized contact distance (d_{norm}), which depends on contact distances to the closest atoms outside (d_e) and inside (d_i) the surface. The 3D d_{norm} surfaces are mapped over a fixed color scale of -0.8273 to 1.0993 a.u. for Co complex. The electrostatic potential was generated using the STO-3G basis set at the Hartree–Fock level of

theory, energy in the range -0.1099 to +0.1470 a.u for water molecule, -0.0543 to +0.1035 a.u for NO_3^- anion and -0.1830 to +0.2303 a.u. for the investigated complex.

2.5. Physical measurements

UV-Visible absorption spectra in dimethyl sulfoxide (DMSO; 10^{-4} M) solvent were recorded in the range 200-900 nm using a SHIMADZU 2450 spectrophotometer. FTIR spectra were recorded on a SHIMADZU FT-IR 8400S spectrometer with samples dispersed in KBr pellets in the range 500-3000 cm^{-1}. Element analyses (C, H and N) were performed on a VARIO-ELEMENTAR analyzer.

Magnetic measurements (thermal dependence of the susceptibility and field dependence of the magnetization) have been collected using the VSM module of a Physical Property Measurement System (PPMS) Dynacool, maximum field = 9T.

2.6. Antifungal and antibacterial activity

The antifungal activity of the title complex was examined against three strains of the fungal plant pathogen *V. dahliae* (Strains SJ, SH and SE) and one strain of the fungal plant pathogen *F. oxysporum* fsp. *melonis* (FOM). Strains of *V. dahliae* were isolated from olive trees in different regions of Morocco while FOM was isolated from a melon field in Doukkala region, Morocco. They were sub-cultured on potato dextrose agar (PDA) plates and incubated at 27 °C in the dark. The cobalt complex was dissolved in 0.2% DMSO and added at concentrations of 5, 50 and 100 μg mL^{-1} to the PDA medium before being autoclaved and cooled. The amended media was poured into Petri dishes and inoculated using 5 mm plugs of agar and mycelium taken from actively growing cultures of fungus on PDA. Petri plates were incubated in the dark at 27°C. The mycelial growth was assessed by measuring 2 orthogonal diameters of each colony after 7 days of incubation. Mycelial growth was compared with growth on PDA amended with

0.2% DMSO (control) and the percentage of inhibition growth was expressed [37] relative to the control. The experiment was repeated 3 times.

The *in vitro* antibacterial activity of the investigated complex was performed against the following phytopathogenic bacteria: *Agrobacterium tumefaciens* (Ach5, A281 and C58 strains), *Pseudomonas syringae* pv. *tabaci* (strain CFBP2106) and *Pseudomonas syringae* pv. *syringae* (strain CFBP692). *A. tumefaciens* strains were sub-cultivated on LB solid medium while *P. syrnigae* pv. *syringae* and *P. syringae* pv. *tabaci* were cultured on King B (KB) medium at 28°C. Antibacterial activities of the dimeric complex was carried out using the agar disc diffusion method as described in [38]. Bacteria that were grown overnight were diluted to a concentration of 3×10^8 CFU. mL^{-1}. Sterile cellulose discs of 6 mm diameter were impregnated with the products (200 µg mL^{-1} in 0.2% DMSO) and discs were placed on either LB or KB solid medium previously amended with 3×10^8 CFU mL^{-1} of bacteria. DMSO (0.2%) was used as a negative control. The inoculated plates were incubated at 28°C for 48 h. The antimicrobial activity was evaluated by measuring the clearance zone around the discs which indicates a positive antibacterial activity of the respective products. Each experiment was repeated 3 times.

All data of antimicrobial activities were expressed as the mean and confidence intervals. They were subjected to ANOVA, and means were compared using Tukey's test and *p* values of 0.05 were considered to be significantly different.

Table 1

Crystal data and summary of the measurement parameters for $[Co_2(bpt)_2(H_2O)_4](NO_3)_2.2H_2O$.

Chemical formula	$C_{12}H_{14}CoN_6O_6$
M_r (g mol^{-1})	397.22
Temperature (K)	296
Wavelength	0.71073 Å
Crystal system, space group	Triclinic, $P\bar{1}$
a, b, c (Å)	9.242(3), 9.327(3), 11.149(4)
α, β, γ (°)	81.067(12), 69.692(12), 60.699(11)
Volume (A^3)	785.8(4)
Z	2
Calculated density (g/cm^3)	1.679
μ (mm^{-1})	1.14
Crystal shape and color	Block, Red
Crystal size (mm)	0.33×0.29×0.25
Data collection	
Diffractometer	'Bruker APEX-II CCD'
Absorption correction	Multi-scan (SADABS)
Theta range for data collection (°)	2.505 – 30.508
Index ranges	-13 ≤ h ≤13, -13 ≤ k ≤13, -15 ≤ l≤ 15
$T_{min,}$ T_{ma}.	0.6621; 0.7464
R_{int}	0.044
Refinement	
Refinement method	Full-matrix least-squares on F^2
Data / restraints / parameters	3996/0/226
$R[F^2 > 2\sigma(F^2)]$, $wR(F^2)$, S	0.031; 0.079, 1.03
H-atom treatment	H atoms parameters constrained
$\Delta\rho_{max}$, $\Delta\rho_{min}$ (e Å^{-3})	0.51, -0.31

Table 2

Selected bond distances (Å) and angles (°) for $[Co_2(bpt)_2(H_2O)_4](NO_3)_2.2H_2O$.

N1–Co1	2.2415 (14)	C6–N4	1.3515 (19)
N2–Co1	2.0506 (13)	C7–N3	1.3279 (18)
O1–Co1	2.0877 (13)	C7–N4	1.3481 (19)
O2–Co1	2.0771 (14)	C8–N5	1.353 (2)
N3–Co1^{i}	2.0505 (13)	C12–N5	1.339 (2)
N5–Co1^{i}	2.2388 (14)	C1–C2	1.385 (2)
C1–N1	1.3386 (19)	C2–C3	1.368 (3)
N2–N3	1.3557 (16)	C3–C4	1.386 (2)
N6–O5	1.231 (2)	C4–C5	1.379 (2)
N6–O6	1.238 (2)	C7–C8	1.475 (2)
N6–O4	1.258 (2)	C8–C9	1.376 (2)
C5–N1	1.3524 (19)	C9–C10	1.391 (2)
C5–C6	1.470 (2)	C10–C11	1.368 (3)
C6–N2	1.3247 (19)		
C1–N1–Co1	128.17 (11)	N3^{i}–Co1–N2	93.35 (5)
C5–N1–Co1	114.45 (9)	N3^{i}–Co1–O2	98.80 (6)
C6–N2–Co1	120.52 (10)	N2–Co1–O2	97.05 (6)
N3–N2–Co1	133.34 (10)	N3^{i}–Co1–O1	90.55 (5)
C7–N3–Co1^{i}	120.58 (10)	N2–Co1–O1	95.16 (6)
N2–N3–Co1^{i}	133.31 (9)	O2–Co1–O1	164.13 (5)
C12–N5–Co1^{i}	127.54 (11)	N3^{i}–Co1–N5^{i}	74.62 (5)
C8–N5–Co1^{i}	114.84 (9)	N2–Co1–N5^{i}	167.88 (5)
N1–C1–C2	122.98 (16)	O2–Co1–N5^{i}	83.67 (6)
C3–C2–C1	119.15 (15)	O1–Co1–N5^{i}	86.52 (5)
C2–C3–C4	118.87 (16)	N3^{i}–Co1–N1	166.86 (5)
C5—C4–C3	118.95 (16)	N2–Co1–N1	74.69 (5)
N1–C5–C4	122.70 (14)	O2–Co1–N1	88.25 (6)
N1–C5–C6	113.65 (13)	O1–Co1–N1	85.23 (5)
C4–C5–C6	123.62 (14)	C6–N2–N3	106.00 (11)
N2–C6–N4	113.41 (12)	C7–N3–N2	105.97 (12)
N2–C6–C5	116.68 (13)	C7–N4–C6	101.22 (12)
N4–C6–C5	129.83 (13)	C12–N5–C8	117.62 (14)
N3–C7–N4	113.39 (12)	O5–N6–O6	120.02 (17)
N3–C7–C8	116.54 (13)	O5–N6–O4	118.25 (17)
N4–C7–C8	130.06 (13)	O6–N6–O4	121.72 (17)
N5–C8–C9	122.66 (14)	O5–N6–O6	120.02 (17)
N5–C8–C7	113.32 (12)	C11–C10–C9	119.25 (16)
C9–C8–C7	124.02 (14)	C10–C11–C12	118.90 (16)
C8–C9–C10	118.61 (16)	N5–C12–C11	122.95 (16)
N1–C5–C4	122.70 (14)	C1–N1–C5	117.36 (13)
N1–C5–C6	113.65 (13)	C4–C5–C6	123.62 (14)

Symmetry code: (i) -*x*+1, -*y*, -*z*+1.

3. Results and discussion

3.1. Crystal structure determination and description

The dinuclear cobalt(II) complex of 3,5-bis(2-pyridyl)-1,2,4-triazolate (bpt), dinitrate dihydrate $[Co_2(bpt)_2(H_2O)_4](NO_3)_2.2H_2O$, crystallizes in triclinic crystal system with $P\bar{1}$ space group and results from the association of the asymmetric unit and its inversion symmetric as illustrated in Fig. 1. The crystallographic study showed that there are two $[Co_2(bpt(H_2O)_4]^{2+}$ cation moieties, two NO_3^- anions and two solvated water molecules in the unit cell. This result indicated that the central triazole ring of Hbpt (ligand) was deprotonated to produce the anionic bpt ligand (Scheme 1). The Co^{II} centres are bridged by the two triazolate moieties and the bpt ligand adopts the cis-(N',N^1,N^2,N'')$_2$ double bridging coordination mode (Scheme 2).

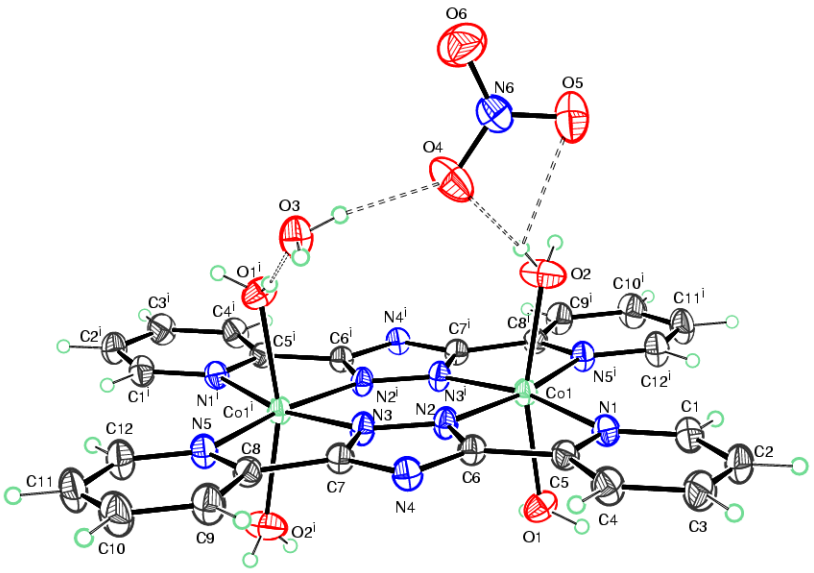

Fig. 1. Plot of the crystal structure of the binuclear cobalt complex, $[Co_2(bpt)_2(H_2O)_4](NO_3)_2.2H_2O$, showing hydration water molecule and nitrate group linked to the complex by hydrogen bonds (dashed lines).

In this complex, the cobalt displays an octahedral N_4O_2 coordination geometry, in which each cobalt ion is linked to four equatorial nitrogen atoms and 2 axial water molecules as co-

ligands completing the distorted octahedron. Indeed, among the 4 nitrogen atoms linked to cobalt there are two which belong to the triazolate rings at distances from Co1–N2 = Co1–N3' = 2.051 (2) Å, very close to the distances between the cobalt and the both water molecules in the axial position Co1–O1 = 2.088 (2) Å and Co1–O2 = 2.077 (2) Å, while the other two nitrogen atoms belonging to the pyridyl rings are located at distances slightly longer namely Co1–N1 = 2.242 (2) Å and Co1–N5'= 2.239 (2) Å and the angle N1–Co1–N5' = 117.42 (5). These values are in agreement with those observed previously which show that generally the M–N bonds with the central ring are significantly shorter than $M–N_{pyridyl}$ [39], which highlights that triazole has probably better electron donating properties than the pyridyl ring [40], which tend to deviate under the electrostatic and steric effects. Instead of an elongated or flat octahedron, these values show that it is an unusually deformation of the cobalt octahedron, but present in other complexes such as the dinuclear nickel(II) complex, $[Ni_2(MOBPT)_2Cl_2(H_2O)_2]Cl_2.7H_2O$ with MOBPT is 4-(p-methoxyphenyl)-3,5-bis(pyridine-2-yl)-1,2,4-triazole [5]. The distortion also causes a slight twist in the bpt ligand which can be seen by examining the angles between the mean plane of the triazolate ring and each of the flanking pyridine rings. The same behaviour was described previously by Prins et al. in the case of Cu^{II} / bpt complexes [19]. On the other hand, the organic part of this complex is almost planar and the largest deviation from the mean plane being 0.2523 Å at $N4^{i}$. The two nitrate groups located on either side of the plane defined by the organic part of the complex balance the molecular charge. Hydration molecules are free water molecules that connect nitrate groups and other water molecules through hydrogen bonds. In this investigated dinuclear complex, the two cobalt centres are 4.170(2) Å apart as shown in Fig. 2. This distance is in good trend with that reported by Klingele et al. in the case of some Co^{II} complexes based on 4-substituted 3,5-di(2-pyridyl)-4H-1,2,4-triazoles as bridging ligands [41]. On the other hand, the shortest interdimer Cu···Cu separation within this network is 8.144(3) Å (Fig. 2). Despite this distance,

the molecules are well interconnected by several hydrogen bonds C–H···O, O–H···O, O–H···N, π–π stacking and O···π (lone-pair···π) interactions as shown in Figs. 3-4. Generally, the lone-pair···π intermolecular interactions are attributed to Coulomb interaction [42].

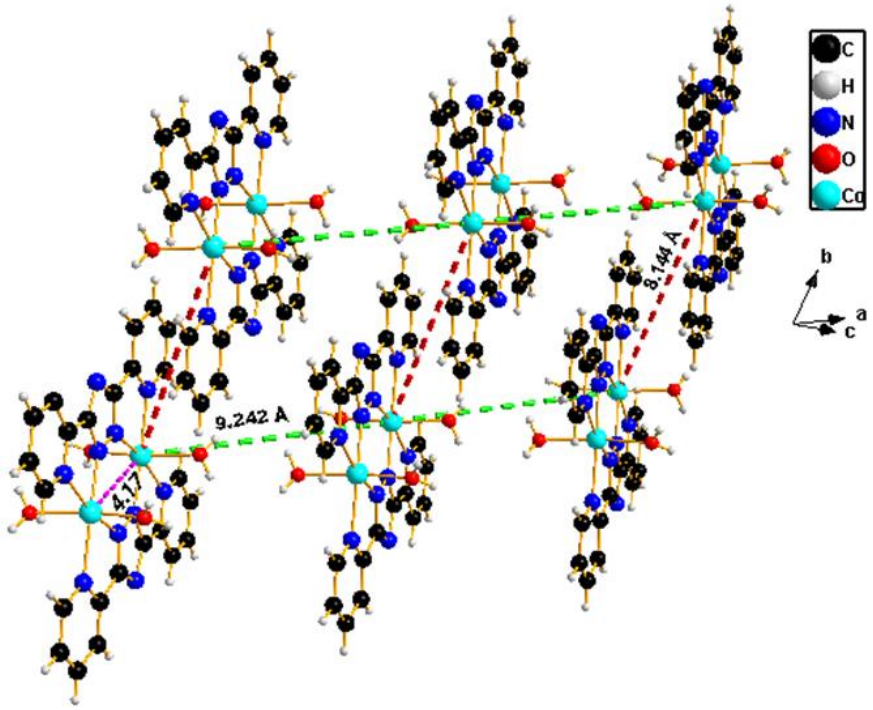

Fig. 2. Projection of the structure of $[Co_2(bpt)_2(H_2O)_4](NO_3)_2.2H_2O$ showing the intra and interdimer Cu···Cu separations.

Indeed, the crystal cohesion is ensured by different O–H···O interactions between solvated and unsolvated water molecules with distances range from 1.93 to 2.00 Å as shown in Fig. 3a and Table 3. Two oxygen atoms of the nitrate groups are also involved in bifurcated hydrogen bonds with the unsolvated water molecules (1.97 - 2.15 Å) and one with the solvated molecule (1.97 Å) as shown in Fig. 1 and Table 3. Moreover, the crystal structure is more stabilized by C–H···O hydrogen bonds between pyridyl rings and non-coordinated NO_3^- conterions with distances varying from 2.53 to 2.58 Å as presented in Fig. 3b. Finally, the stability of the complex structure is reinforced by π–π stacking interactions between the two aromatic pyridyl and triazolate rings (d = 3.968 Å) and also by noncovalently intermolecular

O···π interactions between the lone-pair electrons of O-atom in NO_3^- conteranion and an electron-poor π pyridyl ring of ligand (d = 3.802 Å), as indicated in Fig. 4.

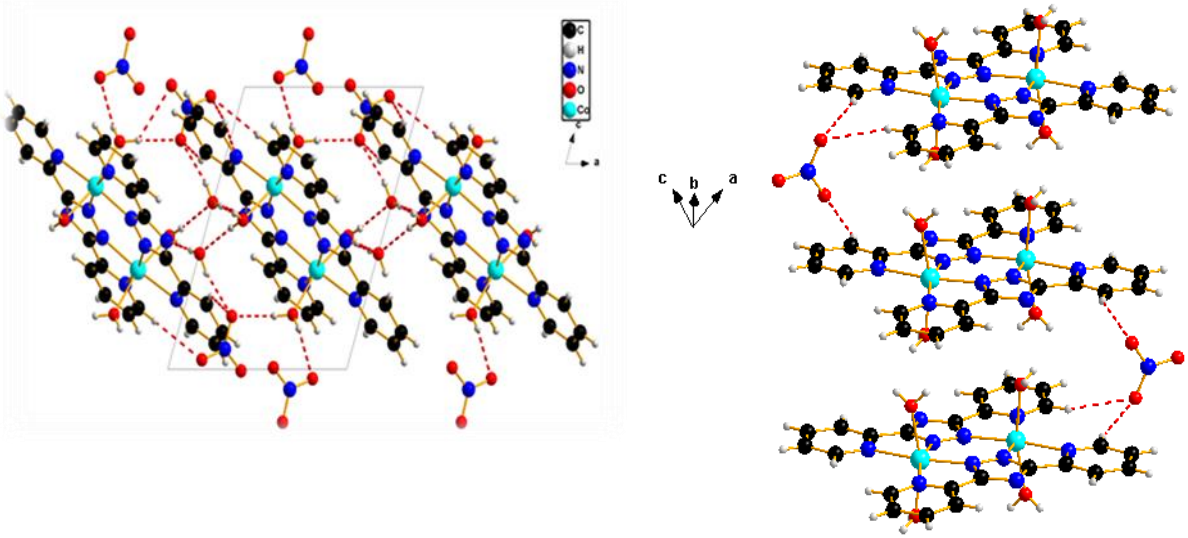

(a) **(b)**

Fig. 3. Three-dimensional crystal structure view of Co complex, showing (a) O–H···O and (b) C–H···O interactions.

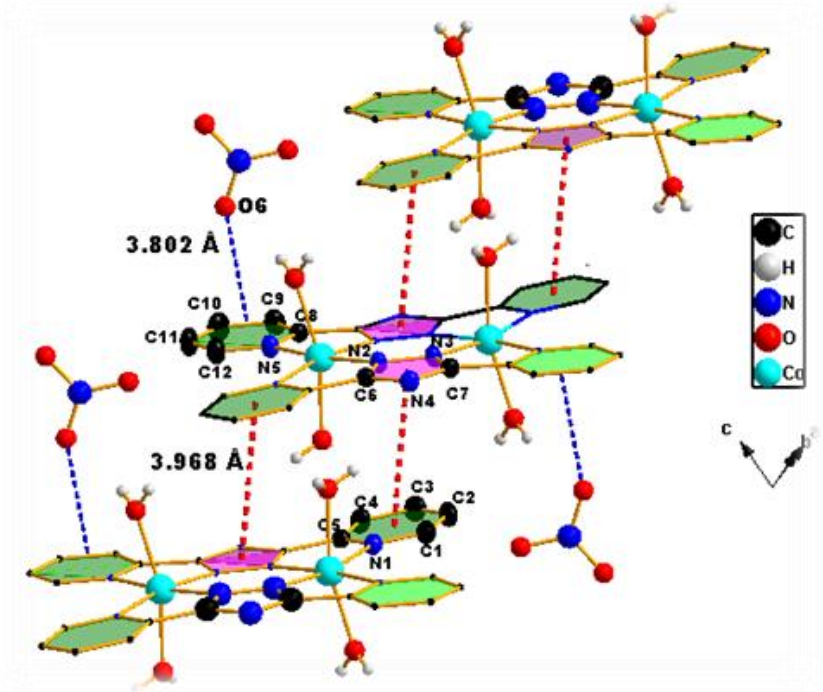

Fig. 4. π–π stacking interactions and O···π intermolecular interactions (between the O-atom of NO_3^- conteranion and pyridyl ring) in crystal structure of $[Co_2(bpt)_2(H_2O)_4](NO_3)_2.2H_2O$.

Table 3

Hydrogen-bond geometry (Å, º) for $[Co_2(bpt)_2(H_2O)_4](NO_3)_2.2H_2O$.

D–H···*A*	*D*–H (Å)	H···*A* (Å)	*D*···*A* (Å)	*D*–H···*A* (°)
C1–H1···O6^{i}	0.9300	2.5800	3.450(3)	156.200
C9–H9···O4^{ii}	0.9300	2.5300	3.324(3)	143.200
C12–H12···O6^{iii}	0.9300	2.5600	3.405(3)	151.500
O2–H2A···O6^{iv}	0.7700	2.1500	2.891(2)	163.000
O2–H2B···O4	0.8400	1.9700	2.801(2)	169.400
O2–H2B···O5	0.8400	2.5300	3.133(2)	129.800
O1–H1A···O3^{v}	0.8000	2.0000	2.7874(18)	169.500
O1–H1B···O3^{i}	0.7900	1.9300	2.7117(17)	173.500
O3–H3A···O4	0.7800	1.9700	2.740(2)	167.800
O3–H3B···N4^{ii}	0.8000	2.0300	2.8331(18)	174.900

Symmetry codes: (i) 1+x, y, z; (ii) -x, 1-y, 1-z; (iii) -x, -y, 1-z; (iv) 1-x, -y, -z; (v) 1-x, -y, 1-z.

3.2. Hirshfeld surface analysis study

The three dimensional d_{norm} surface of $[Co_2(bpt)_2(H_2O)_4](NO_3)_2.2H_2O$ using a standard surface resolution is shown in Figs. 5a-e. The intense red spots on the surface are due to the $H_2O\cdots H–O–H$, $H–O–H\cdots O3_{Nitrate}$ and $H–O–H\cdots N_{triazolate}$ hydrogen bonds resulting from the interactions between the coordinated water and water molecule of crystallization and nitrate group and between the water and N atom of the triazolate ring. On the Hirshfeld surface mapped over the electrostatic potential (Fig. 5f) shows blue regions around the metal coordinating water molecules indicating the positive electrostatic potential, while bright-red spots indicate atoms with negative electrostatic potential. Figs. 5g-h also illustrated the positive and negative electrostatic potential for uncoordinated water molecule (free) and nitrate conterion, respectively.

As illustrated in Fig. 6, the corresponding fingerprint plots for the title compound are shown with characteristic pseudo-symmetric wings in the d_e and d_i diagonal axes and those delineated into H···H, H···O/O···H, C···H/H···C, N···H/H···N and C···C. The relative contributions of all the contacts to the Hirshfeld surface are summarized in Table 4. The presence of water molecules and nitrate ion in the crystal of Co-complex increases the

percentage contribution from O···H/H···O contacts to the Hirshfeld surface of the asymmetric unit compared with the complex molecule alone.

The molecular interactions in terms of H···H contacts are reflected in the distribution of the scattered points in the fingerprint plots, which extend to $d_e = d_i = 1.15$ Å in the Co complex, which comprise 31.6% of the total Hirshfeld surface area (Fig. 6b). The Hirshfeld surface does not show a similar proportion of O···H/H···O with highest contributions of 22.1%, of the total Hirshfeld surface area. In complex, the H···O (19.9% interactions make a larger contribution than the O···H (2.2 %) interactions, corresponding to O–H···O interactions, is represented by the spikes in the bottom right and left region, $d_e + d_i \approx 1.75$ Å (Fig. 6c). In the absence of weak C–H···π interactions in the crystal, the pair of characteristic wings resulting in the fingerprint plot delineated into H···C/C···H contacts with a 18.1% contribution to the Hirshfeld Surface have a symmetrical distribution of points, Fig. 6d, with the tips at $d_e + d_i \approx 3.2$ Å, corresponding to C–H···O (nitrate) interactions. The N···H contacts (8.5%), are represented by two signals with thick edges in the region $d_e + d_i \approx 1.75$ Å (Fig. 6e), which indicates which refer to formation of O–H···$N_{triazolate}$ interactions. The distribution of points in the $d_e = d_i \approx 1.7$ Å range in the fingerprint plot delineated into C···C contacts, indicate the existence of weak π–π stacking interactions between the triazolate rings (N2–N4/C6–C7) and pyridine rings (N1/C1-C5) (Figs. 6f and 7a-b). The presence of the *lp*···π (lone-pair···π) contact in the structure, involving nitrate–O6 and pyridine rings (N5/C8–C12) (Figs. 7a and 7c), is also evident from the contribution of C···O/O···C contacts to the Hirshfeld surface as summarized in Table 4, providing additional stability in 3D architecture.

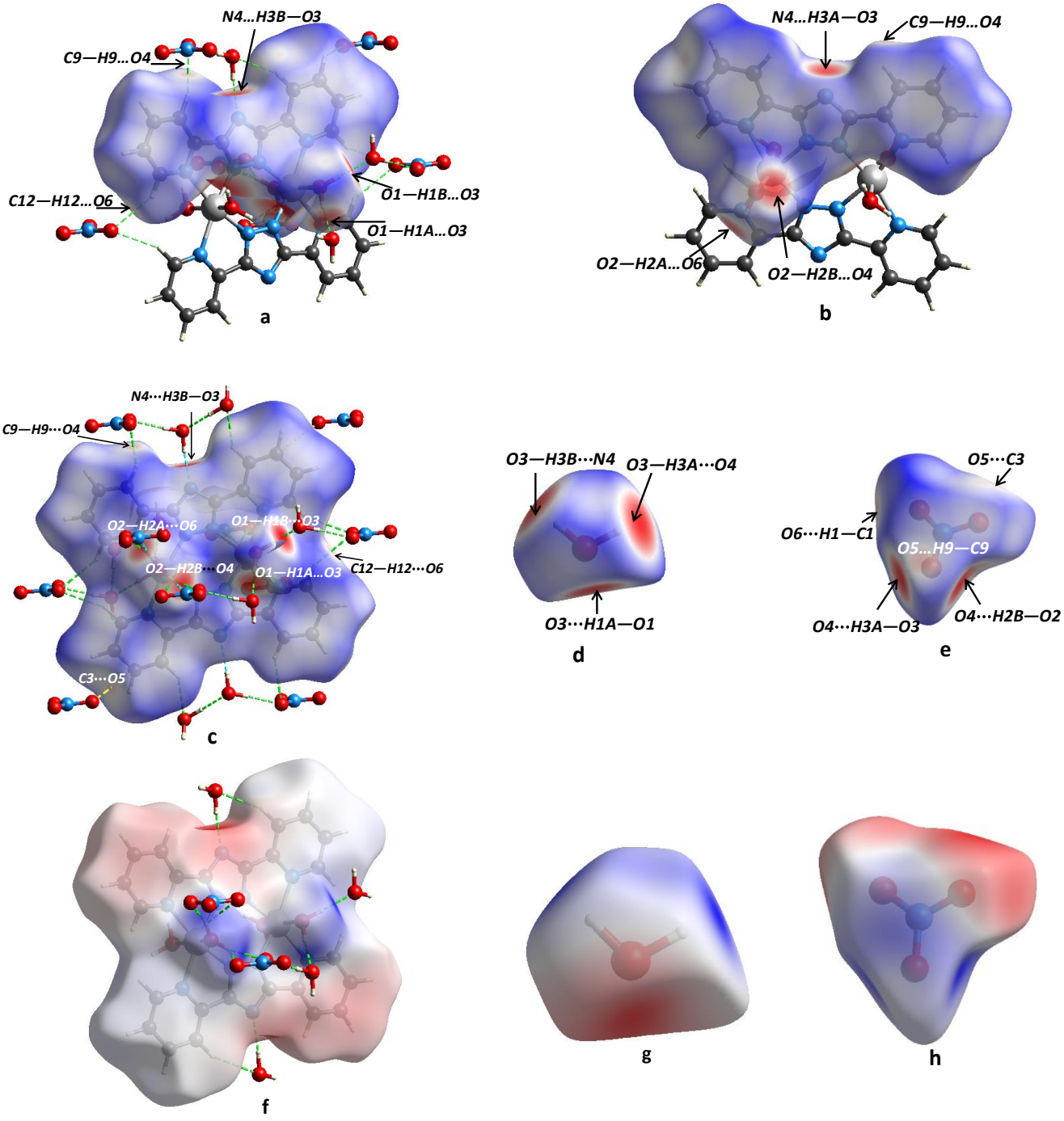

Fig. 5. Viewed Hirshfeld surfaces are shown mapped with d_{norm} of (a) and (b) $[Co(bpt)(H_2O)_2]$, (c) $[Co_2(bpt)_2(H_2O)_4]$**,** (d) Uncoordinated water molecule and (e) NO_3^- conterion. Different views of the Hirshfeld surfaces for the coordinated and the uncoordinated the Co parts mapped over the electrostatic potential: (f) $[Co_2(bpt)_2(H_2O)_4]$ (g) uncoordinated water molecule and (h) NO_3^- conterion.

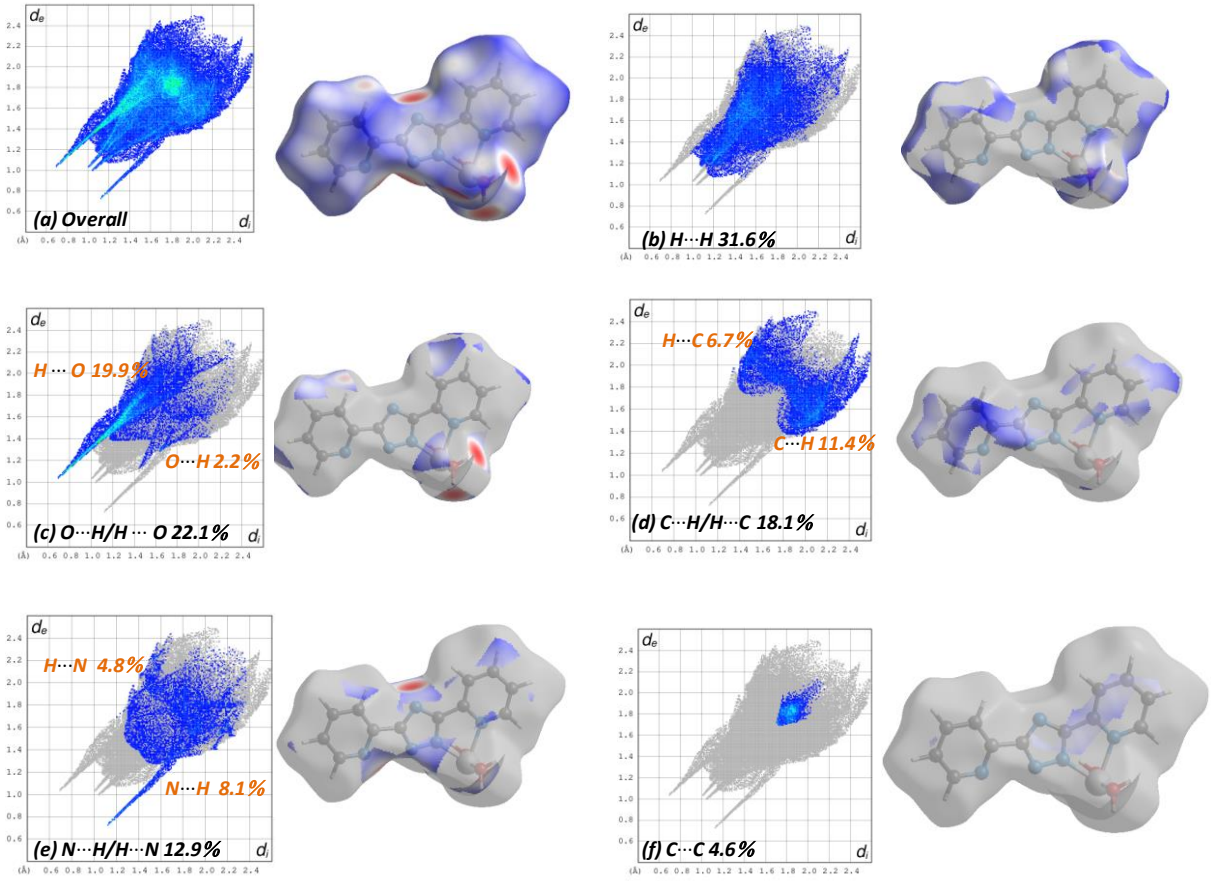

Fig. 6. (a) The two-dimensional fingerprint plot for the title compound, and the fingerprint plots delineated into (b) H···H, (c) O···H/H···O, (d) C···H/H···C, (e) N···H/H···N and (f) C···C contacts.

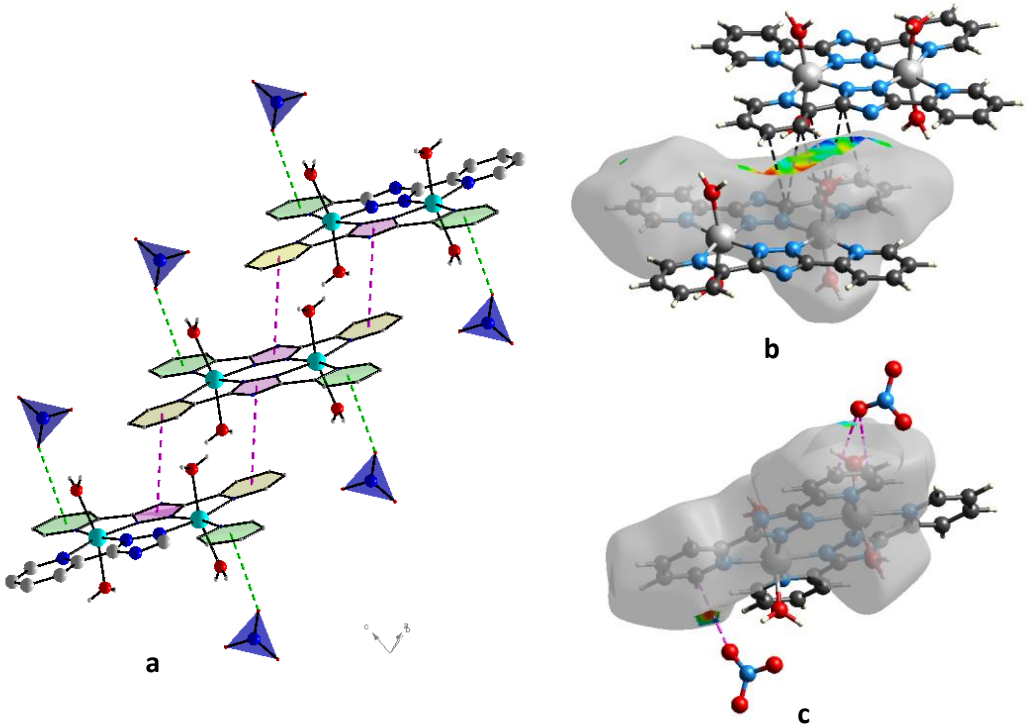

Fig. 7. (a) π–π and $lp\cdots\pi$ interactions in crystal structure of Co complex and views of the Hirshfeld surface mapped with the shape-index property for the complex molecule in (I) from -1.0 to +1.0 a.u. highlighting (b) π–π interaction and (c) the N6–O6$\cdots\pi$ interaction through black and purple dashed lines, respectively.

Table 4
Percentage contributions of interatomic contacts to the Hirshfeld surface for the $Co(bpt)(H_2O)_2$ and $[Co_2(bpt)_2(H_2O)_4](NO_3)_2.2H_2O$.

Contact	Percentage contribution (%)	
	$Co(bpt)(H_2O)_2$	$[Co_2(bpt)_2(H_2O)_4](NO_3)_2.2H_2O$
H···H	31.6	26.7
O···H/H···O	22.1	41.0
C···H/H···C	18.1	17.9
H···N/N···H	12.9	5.4
C···C	4.6	4.4
Co···N/N···Co	5.5	—
C···N/N···C	1.8	1.9
N···O/O···N	1.3	1.1
N···N	1.1	0.3
C···O/O···C	0.9	0.7
H···Co/Co···H	0.2	—

The Hirshfeld surfaces in the coordination geometry formed by the N_4O_2 about the Co(II) centre in the complex molecule that has been mapped to a normal surface are shown in Fig. 8a. The large red and rectangular area on the d_{norm} surface for Co show the contact between N–Co (the bond distances for Co–N vary between 2.051 Å and 2.242 Å) and Co–O (Co–O ≈ 2.077-2.088 Å). The Hirshfeld surfaces of the Co^{2+} ion is much more concave towards the bond directions defined by the O atoms than those associated with coordination towards the N atoms (Figs. 7b and 7c). Although the covalent bonds with the oxygen and nitrogen atoms are dominant (Figs. 8a and 8b), there is weak areas of contact that can be attributed to H···Co interactions. The 2D fingerprint plots of interatomic interactions in the region of cobalt atom (Fig. 8c) indicate that the Co atom has up to 53.2% of the contacts from the Co–N interaction on the Hirshfeld surface (the pair of aligned red points at different inclinations from $d_e + d_i \approx$ 2.0 Å), with 32.2% of the contacts arising from the O–Co coordinates and the remaining 14.6% from H···Co bonds.

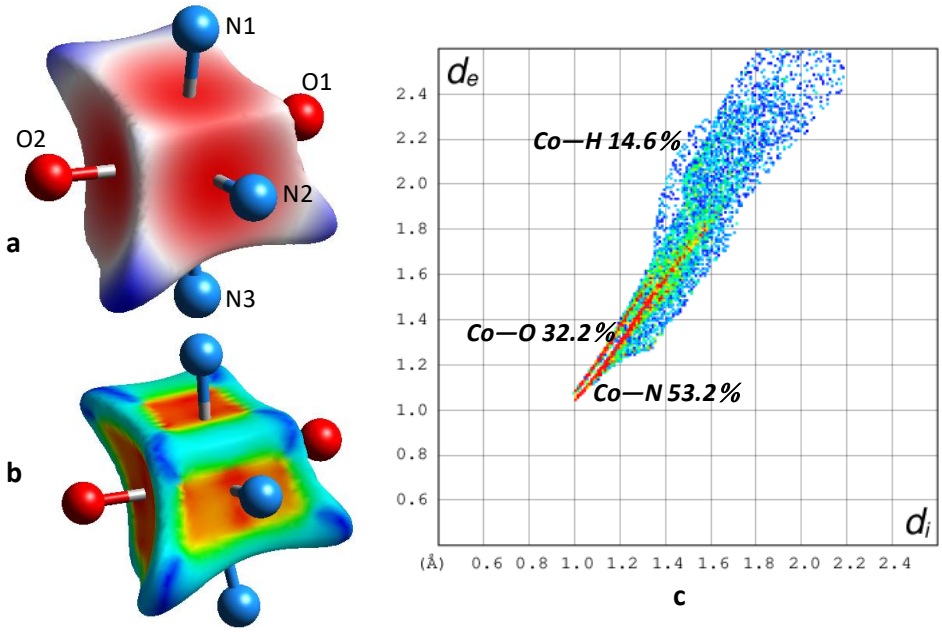

Fig. 8. Atomic Hirshfeld surface of Co in the tittle complex with the descriptor (a) d_{norm}, (b) shape-index mapped onto the surfaces and (c) corresponding fingerprint plot for cobalt.

3.3. Spectroscopy studies

3.3.1. Ultraviolet-visible spectroscopy

The electronic spectra of Hbpt and title complex are shown in Fig. 9. The absorption maxima with the corresponding extinction coefficients are given in Table 5. The UV-Vis spectrum of $[Co_2(bpt)_2(H_2O)_4](NO_3)_2.2H_2O$ in DMSO reveals the presence of two absorption bands in the ultra-violet range at 236 and 260 nm. By analogy with the Hbpt proligand spectrum, these bands were attributed to $\pi \rightarrow \pi^*$ ligand transitions, characteristic of their π-electronic system [40,43]. The significant red shift of the transitions attributed to the ligand in the complex (Table 5) can be due to the stabilization of the π^* orbitals and to a better electronic delocalization along the conjugated system [44]. The *d-d* transitions of the Co complex appear in the visible domain as three low-intensity bands at 479 (λ_1), 509 (λ_2) and 785 nm (λ_3). These maxima correspond respectively to λ_1: $^4T_{1g}$ (F) → $^4T_{1g}$(P), λ_2: $^4T_{1g}$(F) → $^4A_{2g}$(F) and λ_3: $^4T_{1g}$(F) → $^4T_{2g}$(F) transitions for a Co(II) ion in an octahedral geometry [44-47].

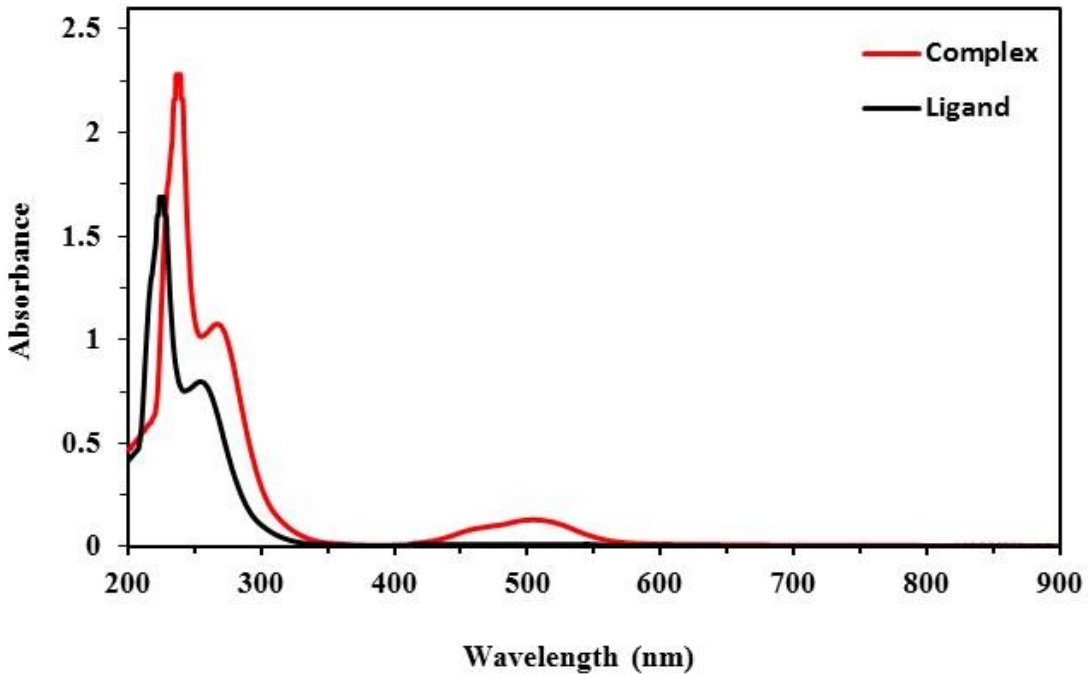

Fig. 9. Electronic spectra of Hbpt ligand and its Co complex.

Table 5
Assignments of the main UV bands of the Hbpt ligand and of its Co complex in DMSO (10^{-4} M).

Compound	λ_{max}, nm (ε_{max}, M^{-1} cm^{-1})				
	$\pi \rightarrow \pi^*$		*d-d*		
			$^4T_{1g}(F) \rightarrow {}^4T_{1g}(P)$	$^4T_{1g}(F) \rightarrow {}^4A_{2g}(F)$	$^4T_{1g}(F) \rightarrow {}^4T_{2g}(F)$
Hbpt	225 (16900)	245 (22800)	—	—	—
Complex	236 (7700)	260 (10600)	479 (1040)	509 (1290)	785 (50)

3.3.2. FTIR spectroscopy

The FTIR spectrum of $[Co_2(bpt)_2(H_2O)_4](NO_3)_2.2H_2O$ is very similar to that of the Hbpt ligand (Fig. 10), except for the presence of a low intensity band around 3400 cm^{-1} and another thinner at 1387 cm^{-1} attributable to water molecules [48,49] and nitrate ions [48,50,51] respectively. The presence of nitrate ions reveals the cationic nature of the product synthesized and the analogy between the two spectra indicates the presence of the ligand in the complex characterized by its main absorption bands, attributable to the (C–H), (C=N) and (C=C) bonds as shown in Table 6.

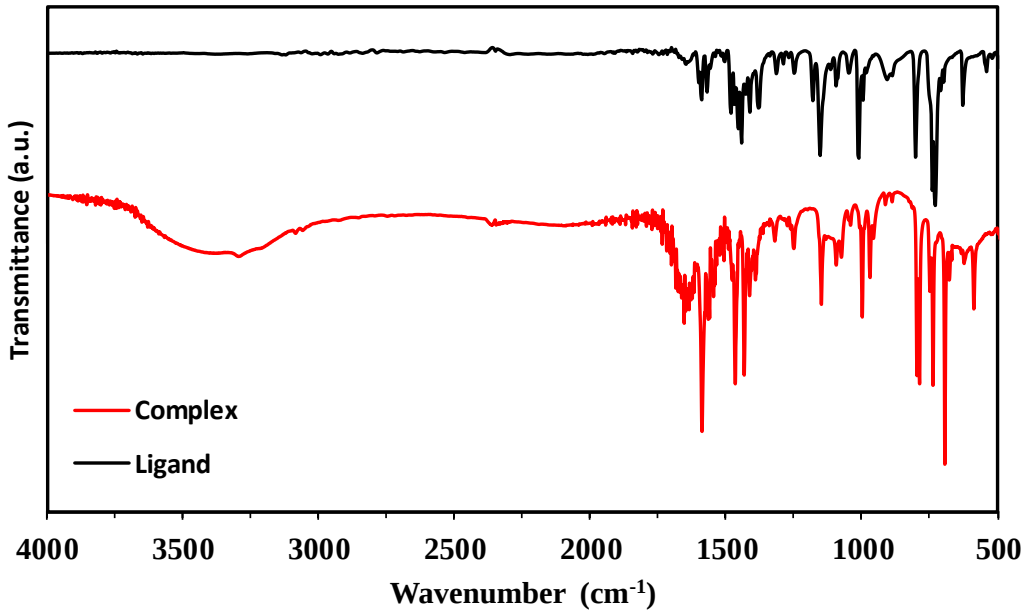

Fig. 10. FTIR spectra of the Hbpt ligand and its Co complex.

Table 6
FTIR data (cm^{-1}) of the Hbpt ligand and its complex.

Compound	ν (NO_3^-)	ν (C=C)	ν (C=N)	ν (C–H)	ν (H_2O)
Hbpt	—	1565 - 1589	1604	3050	—
Complex	1387	1584 - 1600	1636	3066	3400

3.4. Magnetic properties

The temperature dependence of the inversemolar magnetic susceptibility collected at 0.1 T is given in Fig. 11a using one Co^{2+} per formula unit. χ(T) values exhibit a broad maximum at T = 5 K typical of the low-dimensional Co^{2+} dimers units [52]. It also shows ZFC/FC divergence below 7.5 K which signs a minor ferromagnetic impurity responsible for the constant low temperature magnetization of the zero-field cooled (ZFC) branch. This later represents a major drawback for the accurate χ(T) fit (see inset Fig. 11a), signing a weak but real net magnetic moment. The exchange coupling within the dimers was first estimated from the high-temperature Curie-Weiss law fitted between 25 and 400 K (Fig. 11a). We found μ_{eff} =

4.94 μ_B/Co, above the spin-only value of 3.87 μ_B/Co but very close to the commonly reported value *ca.* 4.8 μ_B/Co due to orbital contribution. The *J* exchange between two Co^{2+} ions intra-dimer is J/k_B = -5.6 K using the Curie-Weiss temperature θ = -14.1 K, and $J/k_B = 3\theta/[2S(S+1)]$. This "mean field" approximated solution is expected to give good results in such a "weak *J*" context, compared to other analytical Heisenberg or more accurate Ising solutions and prevails in our study [53]. One must emphasize that the maximal distances between next dimers being > 8.1 Å (Fig. 2), inter-dimer exchanges were neglected. Fig. 10b shows the best fit of the low-temperature χ(T) part using a Ising dimer model after powder averaging of $\chi_{//}$ and $\chi_{\perp}$ [53,54]. For reasons given above there are strong incertitudes on $g_{//}$ and $g_{\perp}$, both scaling the peak height finally fixed. In contrast the temperature of the χ maximum mainly depends on the *J* values giving *J* = -6.61(8) K very close to the Curie-Weiss deductions, revealing weak antiferromagnetic coupling between the two cobalt centers. This value falls in the range usually found for binuclear triazole- and triaolate-N^1,N^2-bridged cobalt complexes [2]. At low temperature, assuming the ferromagnetic extrinsic contribution constant, the Fisher heat capacity given by $d(\chi.T)/dT$ shows a sharp maximum, suggesting magnetic ordering below T_N = 3.11 K (Fig. 11c). Taking into account spatially well isolated dimers, the anisotropy of the Ising dimer exchanges account for such ordering. Finally, the *M*(H) plots are rather informative (Fig. 11d), their evolution is typical of a paramagnetic regime above 7K. Then at 2K, the magnetization turns weaker due to AFM exchanges in the dimers, but abruptly increases above 6.5 T, suggesting a metamagnetic transitions, here the alignment of Co^{2+} in the field is possible until the value 2 μ_B/Co at 9 T.

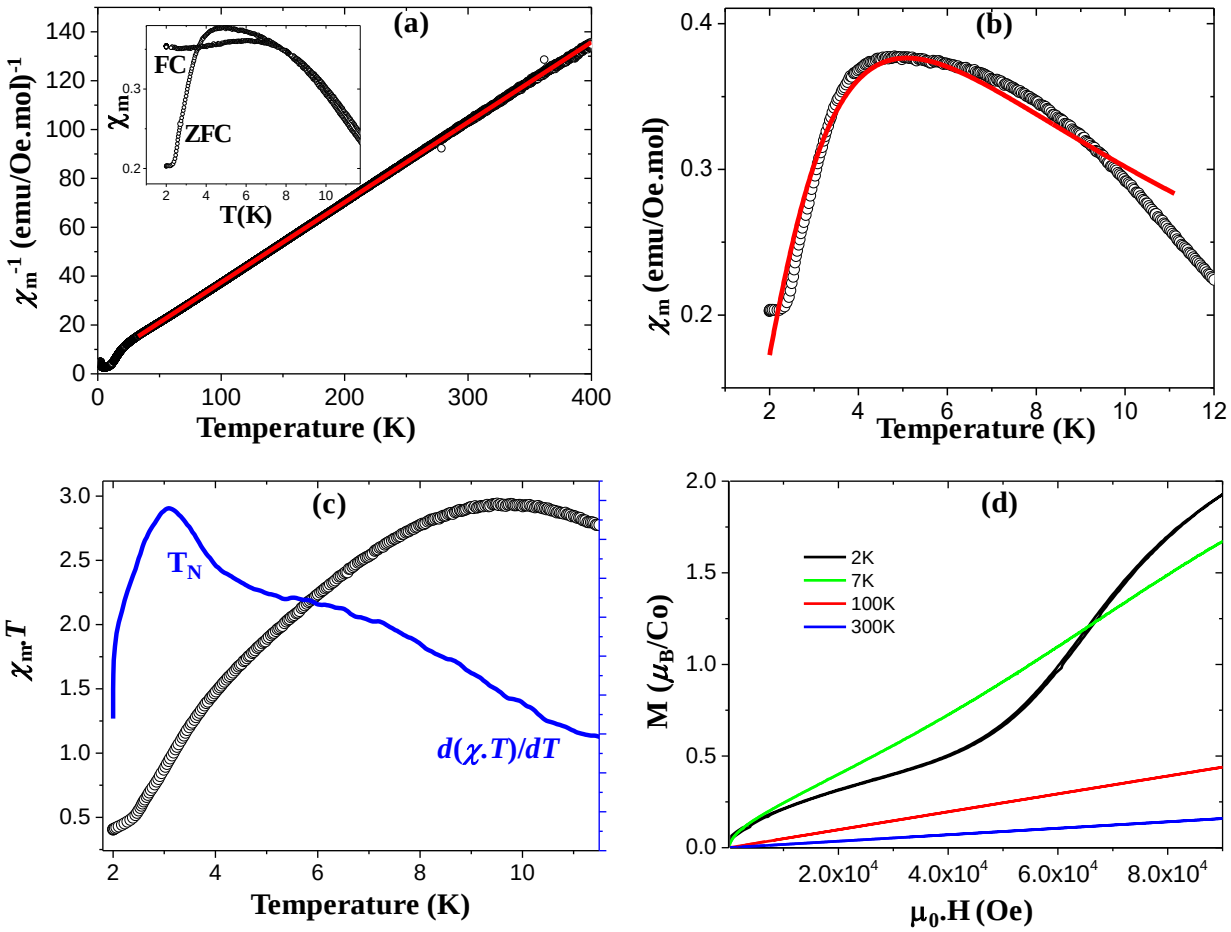

Fig. 11. Temperature dependence of magnetic susceptibility for $[Co_2(bpt)_2(H_2O)_4](NO_3)_2.2H_2O$ measured at 0.1 T in (a) χ_m^{-1} and (b) χ_m forms. The inset in part (a) shows ZFC and FC magnetization curves. Solid lines correspond to the best fit of the experimental data using the Curie-Weiss law in the 25 - 400 K temperature region. (c) Temperature dependence of $\chi_m.T$ for the cobalt complex. (d) Isothermal magnetization of cobalt complex at different temperatures.

3.5. Antimicrobial activities

The effect of $[Co_2(bpt)_2(H_2O)_4](NO_3)_2.2H_2O$ was assessed through the mycelial growth inhibition of three strains of *V. dahliae* and one strain of *F. oxysporum* fsp. *melonis*. *V. dahliae* and *F. oxysporum* are the causal agent of wilt that affects several crops of economic interest [55,56]. Results showed that the investigated dimeric complex exhibited a great antifungal activity against the strains SH and SJ of *V. dahliae* and against *F. oxysporum* fsp. *melonis*. Indeed, at least 70% of inhibition of radial growth was achieved at 50 µg mL^{-1} (Fig. 12a). However, these inhibitions were relatively lowers with the strain SE of *V. dahliae* since only 46 and 66% of inhibition was recorded at 50 and 100 µg mL^{-1}, respectively. Such a differential

sensitivity of these fungal strains to the cobalt complex could be explained by their different genetic background. The elevated activity of this complex may rely on its high lipophilicity allowing its penetration through the lipid bilayer membrane and consequently inhibition of fungal growth. An illustration of the antifungal activity of the dimeric complex against the tested fungal strains was shown in Fig. 12b.

(a)

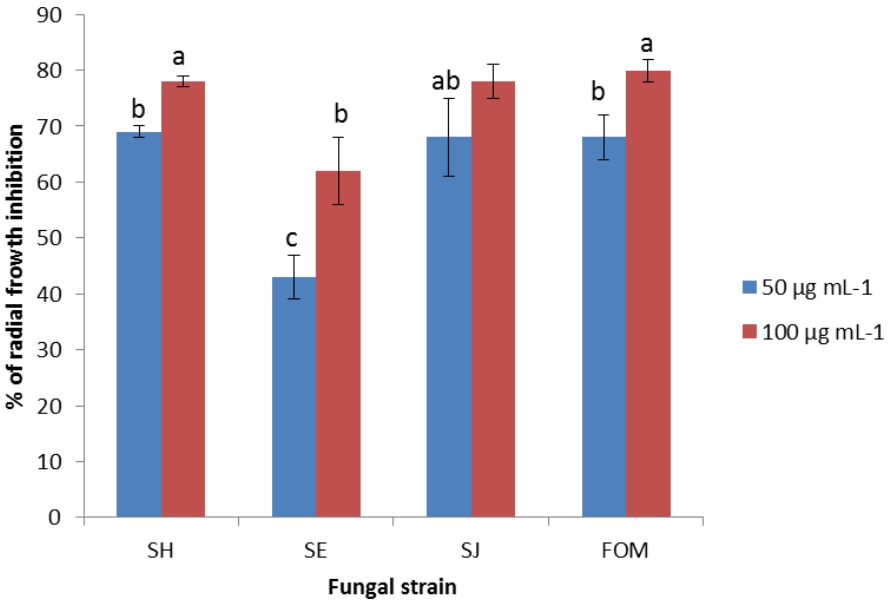

(b)

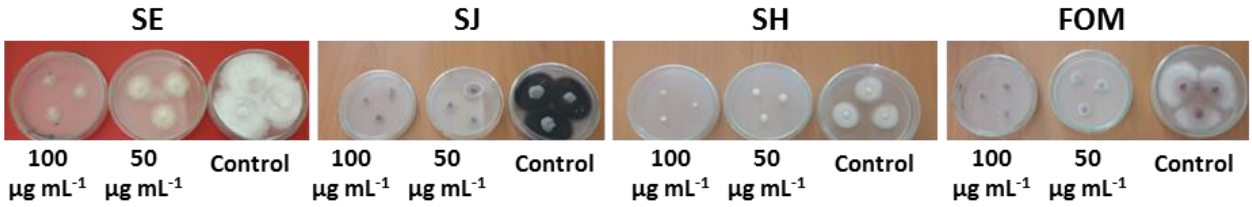

Fig. 12. (a) *In vitro* inhibition of mycelial growth of the strains SH, SE and SJ of *V. dahlia* and of *F. oxysporum* fsp *melonis* (FOM) using the cobalt complex at 50 and 100 µg mL^{-1}. Data are means and confidence intervals from three replicates (α = 5%). Percentage of inhibition growth was determined at 7 days after incubation. Letters indicate significant differences according to Tukey HSD test ($P < 0.55$). (b) Photos showing antifungal activity of the title complex against SE, SJ, SH and FOM.

In this study we also evaluated the effect of the Co^{II} complex against several phytopathogenic bacteria of economic interest including *A. tumefaciens*, the causal agent of crown gall disease [57]. The cobalt complex revealed to effective in the inhibition of the strains A281, C58 and Ach5 (Fig. 13). However, no significant inhibition was recorded for *P. syringae* pv. *tabaci* and *P. syringae* pv. *syringae*, the causal agent of wild fire disease of tobacco and various diseases in several crop [58]. These bacteria are epiphytic and exhibit higher ability to produce form a biofilm allowing them to survive epiphytically. This may explain different sensitivities between tested bacteria. Indeed, the exopolysaccharides (EPS) polymers, which form a capsule involved in biopolymer formation, may act as an effective permeability barrier against the dimeric complex [59].

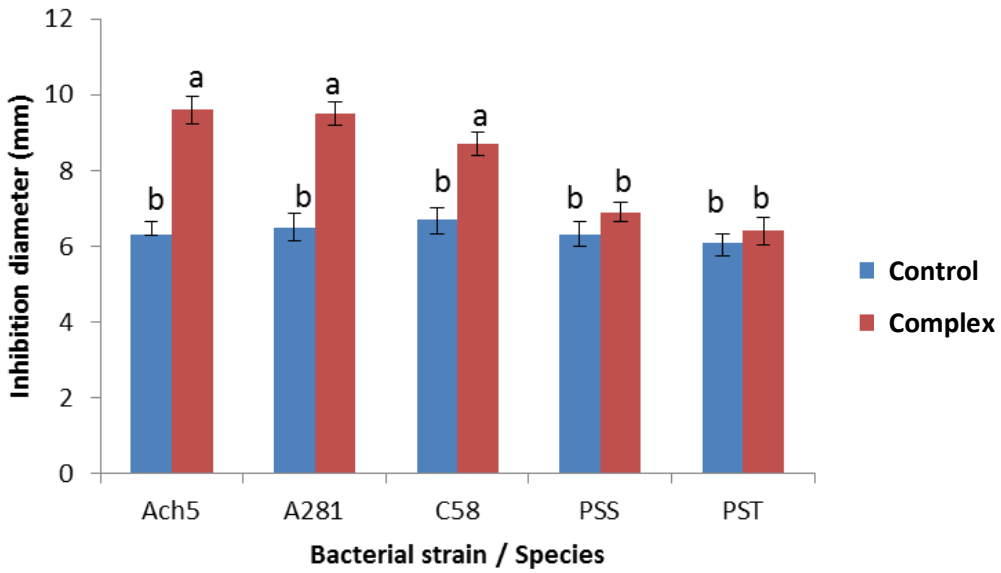

Fig. 13. Antibacterial activity against the strains Ach5, A281 and C58 of *Agrobacterium tumefaciens*, *Pseudomonas syringae*pv. *Syringae* (PSS) and *Pseudomonas syringae*pv. *Tabaci* (PST) using the studied cobalt complex. Data are means and confidence intervals from three replicates (α = 5%). Inhibition diameter was recorded 48 h after incubation at 28 °C with sterile cellulose discs impregnated with 200 µg mL^{-1} of the two products. Letters indicate significant differences according to Tukey HSD test ($P < 0.55$).

4. Conclusions

The reaction of Co^{II} nitrate with Hbpt generates a novel homobimetallic cobalt(II) complex, $[Co_2(bpt)_2(H_2O)_4](NO_3)_2.2H_2O$, and its structure has been characterized by single-crystal X-ray diffraction as well as by UV-Visible and FTIR spectroscopic techniques. The crystal structure determination of Co^{II} complex showed that the dinuclear Co_2N_8 unit is almost planer in which each Co^{II} ion is coordinated by four nitrogen atoms from the anionic ligand (bpt) equatorially and two water molecules axially in a distorted octahedral geometry. The structural stability of the investigated complex results from the establishment of different intermolecular hydrogen bonds, π–π stacking and intermolecular lone-pair$\cdots\pi$ interactions. The 3-D Hirshfeld surface analysis revealed that the cohesion and stabilization of the crystal network is for the most part ensured by means of O···H/H···O (41.0%) intermolecular hydrogen interactions. Magnetic susceptibility study revealed the presence of weak antiferromagnetic exchange coupling between two Co^{II} centers mediated by two central triazolate bridges of bpt ligand. This homobimetallic complex showed also elevated antifungal activity against various strains of phytopathogenic fungus suggesting its possible use as a fungicide in crop protection.

Supplementary material

CCDC 2006865 contains the supplementary crystallographic data for the $[Co_2(bpt)_2(H_2O)_4](NO_3)_2.2H_2O$ complex. These data can be obtained free of charge via www.ccdc.cam.ac.uk/data_request/cif, or by emailing data_request@ccdc.cam. ac.uk, or by contacting the Cambridge Crystallographic Data Centre, 12 Union Road, Cambridge CB2 1EZ, UK; fax: +44 1223 336033.

Acknowledgements

CUR CA2D of Chouaib Doukkali University is acknowledged for its technical support and UATRS-CNRST for the use of the Bruker X8 diffractometer. The Fonds Européen de Développement Régional (FEDER) and contrat plan état région (CPER), CNRS, Région Hauts-de-France and Chevreul Institute (FR 2638) are also acknowledged for funding of the Physical Property Measurement System (PPMS). We thank Laurence Claire Minaud for her magnetic experimental contribution.

Reference

[1] X.-H. Bu, H. Liu, M. Du, L. Zhang, Y.-M. Guo, M. Shionoya, J. Ribas, Inorg. Chem. 41 (2002) 1855–1861.
[2] U. Beckmann, S. Brooker, Coord. Chem. Rev. 245 (2003) 17–29.
[3] M.H. Klingele, S. Brooker, Coord. Chem. Rev. 241 (2003) 119–132.
[4] L. Cheng, W.-X. Zhang, B.-H. Ye, J.-B. Lin, X.-M. Chen, Inorg. Chem. 46 (2007) 1135–1143.
[5] J. Zhou, J. Yang, L. Qi, X. Shen, D. Zhu, Y. Xu, Y. Song, Transit. Met. Chem. 32 (2007) 711–715.
[6] M.-L. Tong, C.-G. Hong, L.-L. Zheng, M.-X. Peng, A. Gaita-Ariño, J.M. Clemente Juan, Eur. J. Inorg. Chem. (2007) 3710–3717.
[7] J.A. Kitchen, S. Brooker, Coord. Chem. Rev. 252 (2008) 2072–2092.
[8] C. Adhikary, S. Koner, Coord. Chem. Rev. 254 (2010) 2933–2958.
[9] F. Bentiss, M. Lagrenée, O. Mentre, P. Conflant, H. Vezin, J.P. Wignacourt, E.M. Holt, Inorg. Chem. 43 (2004) 1865–1873.
[10] A. Laachir, S. Guesmi, M. Saadi, L. El Ammari, O. Mentre, H. Vezin, S. Colis, F. Bentiss, J. Mol. Struct. 1123 (2016) 400–406.
[11] M. Outirite, B. Mernari, F. Bentiss, F. Capet, M. Lagrenée, J. Mol. Struct. 989 (2011) 60–69.
[12] G. Aromí, L.A. Barrios, O. Roubeau, P. Gamez, Coord. Chem. Rev. 255 (2011) 485–546
[13] D. Mulhern, S. Brooker, H. Gorls, S. Rau, J.G. Vos, Dalton Trans. (2006) 51-57.
[14] J.-C. Chen, S. Hu, A.-J. Zhou, M.-L. Tong, Y.-X. Tong, Z. Anorg. Allg. Chem. 632 (2006) 475-481.
[15] J.-C. Chen, A.-J. Zhou, S. Hu, M.-L. Tong, Y.-X. Tong, J. Mol. Struct. 794 (2006) 225-229.
[16] M. Maekawa, K. Sugimoto, T. Okubo, T. Kuroda-Sowa, M. Munakata, Inorg. Chim. Acta 426 (2015) 64–70
[17] H.L.C. Feltham, A.S. Barltrop, S. Brooker, Coord. Chem. Rev. 344 (2017) 26–53.
[18] J.-P. Zhang, Y.-Y. Lin, X.-C. Huang, X.-M. Chen, J. Am. Chem. Soc. 127 (2005) 5495–5506.
[19] R. Prins, P.J.M.W.L. Birker, J.G. Haasnoot, G.C. Verschoor, J. Reedijk, Inorg. Chem. 24 (1985) 4128–4133.
[20] Z.-S. Meng, L. Yun, W.-X. Zhang, C.-G. Hong, R. Herchel, Y.-C. Ou, J.-D. Leng, M.-X. Peng, Z.-J. Lina, M.-L. Tong, Dalton Trans. (2009) 10284–10295.
[21] R. Hage, J.G. Haasnoot, H.A. Nieuwenhuis, J. Reedijk, D.J.A.D. Ridder, J.G. Vos, J. Am. Chem. Soc. 112 (1990) 9245-9251.
[22] D.M. D'Alessandro, P.H. Dinolfo, J.T. Hupp, P.C. Junk, F.R. Keene, Eur. J. Inorg. Chem. (2006) 772-783.
[23] K. Singh, M.S. Barwa, P. Tyagi, Eur. J. Med. Chem. 42 (2007) 394–402.
[24] G.B. Bagihallia, P.G. Avaji, S.A. Patila, P.S. Badami, Eur. J. Med. Chem. 43 (2008) 2639–2649.
[25] A.K. Singh, O.P. Pandey, S.K. Sengupta, Spectrochim. Acta A 85 (2012) 1–6.
[26] F. Gao, T. Wang, J. Xiao, G. Huang, Eur. J. Med. Chem. 173 (2019) 274–281.
[27] J. F. Geldard, F. Lions, J. Org. Chem. 30 (1965) 318–319.
[28] Bruker, SAINT. Bruker AXS Inc., Madison, Wisconsin, USA, 2012.
[29] L. Krause, R. Herbst-Irmer, G.M. Sheldrick, D. Stalke, J. Appl. Cryst. 48 (2015) 3–10.
[30] G.M. Sheldrick, Acta Cryst. A71 (2015) 3–8.
[31] G.M. Sheldrick, Acta Cryst. C71 (2015) 3–8.
[32] L.J. Farrugia, J. Appl. Cryst. 45 (2012) 849–854.
[33] C.F. Macrae, I.J. Bruno, J.A. Chisholm, P.R. Edgington, P. McCabe, E. Pidcock, L. Rodriguez-Monge, R. Taylor, J. van de Streek, P.A Wood, J. Appl. Cryst. 41 (2008) 466–470.
[34] M.A. Spackman, D. Jayatilaka, CrystEngComm 11 (2009) 19–32
[35] J.J. McKinnon, D. Jayatilaka, M.A. Spackman, Chem. Commun. (2007) 3814–3816.
[36] M.J. Turner, J.J. McKinnon, S.K. Wolff, D.J. Grimwood, P.R. Spackman, D. Jayatilaka, M.A. Spackman, CrystalExplorer17, The University of Western Australia, 2017.
[37] A. Smaili, N. Mazoir, L.A. Rifai, T. Koussa, K. Makroum, A. Benharref, L. Faize, N. Alburquerque, L. Burgos, M. Belfaiza, M. Faize (2017). Nat. Prod. Commun. 12 (2017) 331–336.
[38] S. Esserti, A. Smaili, LA. Rifai, T. Koussa, K. Makroum, M. Belfaiza, M. Kabil, L. Faize, L. Burgos, N. Alburquerque, M. Faize, J. Appl. Phycol. 29 (2017) 1081–109.

[39] Y.-W. Zhang, G. Zhang, Y.-Y. Sun, L. Cheng. Acta Cryst. E64 (2008) m1073.
[40] D. Schweinfurth, S. Strobel, B. Sarkar, Inorg. Chim. Acta 374 (2011) 253–260.
[41] M.H. Klingele, P.D.W. Boyd, B. Moubaraki, K.S. Murray, S. Brooker, Eur. J. Inorg. Chem. (2006) 573–589.
[42] Z.-F. Tian, H.-B. Duan, H. Zhou, X.-M. Ren, H. Zhang, Q.-J. Meng, Inorg. Chem. Commun. 12 (2009) 148–150.
[43] H. M. Burke, J.F. Gallagher, M.T. Indelli, J.G. Vos, Inorg. Chim. Acta 357 (2004) 2989–3000.
[44] F. Rhoufal, A. Laachir, S. Guesmi, L. Jouffret, N. Sergent, S. Obbade, M. Akkurt, F. Bentiss, ChemistrySelect 4 (2019) 7773–7783.
[45] N. Raman, A. Kulandaisamy, A. Shunmugasundaram, K. Jeyasubramanian, K. (2001). Transit. Met. Chem. 26 (2001) 131–135.
[46] S.C. Manna, S. Mistri, E. Zangrando, Inorg. Chim. Acta 413 (2014) 166–173.
[47] A. Laachir, F. Rhoufal, S. Guesmi, E.M. Ketatni, L. Jouffret, E. Hlil, N. Sergent, S. Obbade, F. Bentiss, J. Mol. Struct. 1208 (2020) 127892.
[48] Z.K. Khoramdareh, S.A. Hosseini-Yazdi, B. Spingler, A.A. Khandar, Inorg. Chim. Acta 415 (2014) 7–13.
[49] T. Zhang, H.Q. Huang, H.X. Mei, D.F. Wang, X.X. Wang, R.B. Huang, L.S. Zheng, J. Mol. Struct. 1100 (2015) 237–244.
[50] M.A. Abu-Youssef, V. Langer, L. Ohrstrom, Dalton Trans. 21 (2006) 2542–2550.
[51] A.A.A. Massoud, A. Hefnawy, V. Langer, M.A. Khatab, L. Ohrstrom, M.A. Abu-Youssef, Polyhedron 28 (2009) 2794–2802.
[52] R.L. Carlin, Magnetochemistry, Springer, Heidelberg, 1986.
[53] V. Spasojevic, V. Kusigerski, S.P. Sovilj, J. Mrozinski, J. Magn. Magn. Mater. 219 (2000) 269–274.
[54] E. Coronado, M. Drillon, P. R. Nugteren, L. J. De Jongh, D. Beltran, J.Am. Chem. Soc. 110 (1988) 3907–3913.
[55] T.R. Gordon, R.D. Martyn, Annu. Rev. Phytopathol. 35 (1997) 111–128
[56] H. Zine, LA. Rifai, T. Koussa, F. Bentiss, S. Guesmi, A. Laachir, K. Makroum, M. Belfaiza, M. Faize, Pest Man. Sci. 73 (2017) 188–197
[57] E.E. Hood, G.L. Helmer, R.T. Fraley, M.D. Chilton. J. Bact. 186 (1986) 1291–1301.
[58] C. Morris, C.L. Monteil, O. Berge, Ann. Rev. Phytopat. 51 (2013) 85–104.
[59] M. Mukesh, S. Prashant, Z. Andleeb, A. Mohd, K.D. Manish, B.P. Chandra, R.S. Upadhyay, Biotechnol. Bioeng. (2019) 181–208.